Soil Dynamics and Earthquake Engineering 122 (2019) 67–78

Contents lists available at ScienceDirect

Soil Dynamics and Earthquake Engineering

journal homepage: www.elsevier.com/locate/soildyn

3D viscoelastic full waveform inversion of seismic waves for geotechnical site investigation

Majid Mirzanejad, Khiem T. Tran*

University of Florida, Department of Civil and Coastal Engineering, 365 Weil Hall, P.O. Box 116580, Gainesville, FL, 32611, USA

ARTICLE INFO

Keywords:
3D viscoelastic full waveform inversion
Geotechnical site characterization
Surface-based waveform tomography
Quality factor

ABSTRACT

Full waveform inversion (FWI) methods are becoming efficient geophysical tools for geotechnical site investigation. They rely on a mathematical description of wave propagation phenomena to generate synthetic wave-fields, which are then matched with measured wave-fields for extraction of material properties. Due to the inherent computational challenges in implementing a viscoelastic treatment of the wave propagation phenomena, most of the existing 3D FWI algorithms are based on an elastic treatment, and hence ignore the anelastic behavior of materials. The focus of this study is to account for the anelastic effect of materials in the inversion analysis to improve inverted results. Therefore, a 3D viscoelastic FWI method is developed and tested on synthetic and field datasets. The method is based on an existing solution of 3D viscoelastic wave equations (finite-difference solver SOFI3D) and the adjoint-state inversion approach. The results show that the viscoelastic waveform analysis was able to characterize low- and high-velocity synthetic layers, and real variable soil layers. The S-wave velocity (*Vs*) profiles from field experiment generally agree with invasive standard penetration test (SPT) N-values, including identification of a low-velocity zone. *Vs* profiles obtained from a 3D elastic FWI are also included for comparison, and results from the viscoelastic inversion are more consistent with the SPT N-values in both trend and magnitudes.

1. Introduction

Inversion techniques provide a powerful and efficient tool to extract information of subsurface stratigraphy and material properties using seismic data. Surface-based methods such as multichannel analysis of surface waves (MASW), refraction tomography, and full waveform tomography have gained popularity in the past few decades due to their cost-effective implementation in the field. With the rapid advancement in computer technology and processing power, the full waveform tomography has been in the spotlight in the past decade due to its higher resolution and accuracy in characterizing subsurface features [31].

Several 3D full waveform inversion (FWI) algorithms have been developed for large-scale inverse problems [1,7,11,14,17,21,24,26,30,32]. At large scales (kilometers), surface waves can be separated from body waves and removed from waveform analysis. The removal of the surface waves allows for better resolving of deeper structures and reducing inversion artifacts. On the other hand, at small scales (meters), it is difficult to remove the surface waves from the analysis, and they often produce very large model updates (overshooting) that lead to inversion artifacts at shallow depths. There are also other inherent challenges that have hindered the widespread use of FWI in near-surface geophysical applications. Some of these as mentioned by Tran and Luke [29] include inconsistent wave excitation, strong attenuation due to anelastic effects, strong variability of near surface lithology, and insufficient a priori knowledge of the subsurface features that create challenges in the implementation of a robust inversion algorithm.

Most of the works carried out so far on 3D FWI techniques use acoustic wave equations to simulate wave propagation. Even though, the acoustic wave simulation is suitable for inverting marine hydrophone data, it usually falls short of describing land seismic data due to ignoring elastic effects or the contribution of shear waves [4]. The elastic effects must be accounted for a realistic representation of actual land-based field seismograms. There have been a few 3D FWI studies on synthetic and field data [4,9,10,19] that use elastic wave equations to simulate wave propagation. Using the elastic wave simulation, it is possible to account for the geometric spreading and scattering events at heterogeneities that cause attenuation of the wave energy as it propagates away from the source.

However, the elastic simulation is not sufficient to describe attenuation due to intrinsic absorption by the material anelasticity [12]. Viscoelastic formulations as described by Carcione et al. [5] and

* Corresponding author.
E-mail addresses: m.mirzanejad@ufl.edu (M. Mirzanejad), ttk@ufl.edu (K.T. Tran).

https://doi.org/10.1016/j.soildyn.2019.04.005
Received 21 October 2018; Received in revised form 2 April 2019; Accepted 3 April 2019

Robertsson et al. [23] have the advantage of accounting for this intrinsic absorption. Furthermore, anelastic effects can alter the shape of waveform not merely in terms of amplitude and phase, but also in terms of wave mode conversions from P-wave to S-wave and vice versa as described by Robertsson et al. [23]. Ignoring the anelastic effects may lead to inaccurate model updating, inversion artifacts, and consequently possible loss of information from the final inverted result.

Work on viscoelasticity dates back to the nineteenth century with the emergence of constitutive mechanical models. The models consist of a spring and a dashpot in various configurations to explain the time related strain rate and the nonlinear stress-strain behavior as observed in some materials. The standard linear solid and the generalized Maxwell model are two examples of such mechanical models proposed to describe creep and stress relaxation phenomena. The time dependence of strain and stress and the nonlinear stress-strain relationship as observed from experiments, which requires the definition of a time-dependent material modulus, have had wide-spread implications in developing constitutive relations of wave propagation in viscoelastic materials.

Viscoelastic wave equations are based on the conservation of momentum and a description of the time-dependent material behavior. One complication that arises in the formulation of the viscoelastic wave equations compared to that of the elastic equations is the existence of convolution integrals in the stress-strain relation, which makes it less amenable to a numerical approach. Carcione et al. [5] were the first to introduce memory variables to circumvent the convolution integrals. This adds another set of equations that needs to be numerically solved to obtain the memory variables as a function of time and for each relaxation mechanism. The result is a more accurate description of the wave propagation phenomena in real media at the cost of added computation time, which due to the advancement in processing power and parallelization technologies is becoming ever more feasible.

There have been very few studies on viscoelastic FWI on synthetic and field data. In recent studies reported by Wang et al. [33] and Trinh et al. [28], 3D viscoelastic FWI methods were developed and successfully demonstrated on synthetic data at km-scales. At smaller scales, a 2D viscoelastic FWI [13] was used to recover subsurface features in a predominantly depth dependent (1D) structure using a reflection acquisition geometry of a single line of sources and receivers. In another study reported by Fabien-Ouellet et al. [8], a 2D viscoelastic FWI was used on synthetic seismograms from a cross-hole acquisition geometry to appraise its merits on inversion results in a high attenuation scenario, where CO_2 injection is tracked over time. Lastly, Dokter et al. [6] successfully used a 2D viscoelastic FWI to invert SH- and Love-wave data, and compared results to that of an elastic inversion. However, with a high Q value of 15 from the measured data, they found that the influence of anelastic effects on the inversion result was rather small. To the best of the authors' knowledge, studies of 3D viscoelastic FWI on field data at small scales (less than 30 m in depth) are still non-existent.

The focus of this paper is to develop a 3D viscoelastic FWI algorithm for geotechnical site investigation, more specifically for characterization of subsurface stratigraphy (layer interface) and soil/rock properties (S-wave and P-wave velocities, *Vs* and *Vp*) using seismic data. The algorithm is applied to synthetic and field data for assessment of anelastic effects on inversion results. Using an amplitude versus offset (AVO) analysis, we obtain a single value for the quality factor (Q) of the P- and S-waves that best describes the overall anelasticity of the medium with respect to the field data. This Q value is kept constant, and only velocity parameters *Vs* and *Vp* are updated during the inversion process. The inversion results of the field data are compared with those from the 3D elastic FWI [19], and improvements in recovering subsurface features are discussed.

2. Viscoelastic full waveform inversion implementation

The presented 3D viscoelastic FWI is comprised of 1) the forward modelling to generate synthetic seismograms, and 2) the optimization algorithm to minimize the misfit between the synthetic and observed seismograms for extraction of material properties. The forward simulation is based on the viscoelastic finite-difference solver (SOFI3D code), and the steepest descent gradient approach is used to minimize the misfit function. The viscoelastic parameter, or the quality factor Q, defines the level of intrinsic attenuation in the medium and is determined by an AVO (amplitude versus offset) comparison of the synthetic versus field data. The process is elaborated in the following subsections.

2.1. Forward modelling of 3D viscoelastic wave propagation

3D viscoelastic wave propagation in anelastic media is described by a set of the first-order linear partial differential equations. These consist of constitutive relationships denoting the rheology of the medium, and equations for the memory variables and particle velocities [3,5,23] as:

$$\begin{aligned}
&\dot{\sigma}_{ij} = \frac{\partial v_k}{\partial x_k}(M(1+\tau^p) - 2\mu(1+\tau^p)) + 2\frac{\partial v_i}{\partial x_j}\mu(1+\tau^s) + \sum_{l=1}^{L} r_{ijl} \quad for \quad i = j\\
&\dot{\sigma}_{ij} = \left(\frac{\partial v_i}{\partial x_j} + \frac{\partial v_j}{\partial x_i}\right)\mu(1+\tau^s) + \sum_{l=1}^{L} r_{ijl} \quad for \quad i \neq j\\
&\dot{r}_{ijl} = -\frac{1}{\tau_{\sigma l}}\left((M\tau^p - 2\mu\tau^s)\frac{\partial v_k}{\partial x_k} + 2\frac{\partial v_i}{\partial x_j}\mu\tau^s + r_{ijl}\right) \quad for \quad i = j\\
&\dot{r}_{ijl} = -\frac{1}{\tau_{\sigma l}}\left(\mu\tau^s\left(\frac{\partial v_i}{\partial x_j} + \frac{\partial v_j}{\partial x_i}\right) + r_{ijl}\right) \quad for \quad i \neq j\\
&\dot{v}_i = \frac{1}{\rho}\left(\frac{\partial \sigma_{ij}}{\partial x_j} + f_i\right)
\end{aligned} \tag{1}$$

In the above equations, σ_{ij} denotes the *ij*-th component of the stress tensor, v_i denotes the *i*-th component of the particle velocities, r_{ijl} are the memory variables for each relaxation mechanism denoted by the subscript *l*. The stress tensor, particle velocities, and memory variables are functions of spatial coordinates (x, y, and z) and time. The dot over a variable denotes its derivative with respect to time. The external body force (f_i) is only applied at source locations, and $\tau_{\sigma l}$ are the relaxation time for each relaxation mechanism *l*. *M* is the attenuative modulus for P-waves, $M = \lambda + 2\mu$ (λ and μ are the attenuative Lame's parameters), μ is also the attenuative modulus for S-waves, and ρ is the density. The moduli and density are material properties, which are functions of spatial coordinates (x, y, and z) and independent of time. Constants τ^p, τ^s are the attenuation levels for P- and S-waves determined from the quality factors Qp and Qs for P- and S-waves [3,23] as:

$$\tau^p = \frac{2}{Qp} \quad and \quad \tau^s = \frac{2}{Qs} \tag{2}$$

We use the SOFI3D code (https://git.scc.kit.edu/GPIAG-Software/SOFI3D/) for the forward modelling in this study. Details on the forward modelling implementation including the finite-difference scheme, boundary conditions, and parallelization can be found in Ref. [3].

There are at least three mechanisms that can be used to explain wave energy dissipation in real media. The first and the most well-known mechanism is through geometric spreading, which affects wave energy and particle displacement amplitude as a function of time and space. Another less studied mechanism is through scattering of the propagating waves and the subsequent mode conversions of the reflected and refracted waves at heterogeneities. Both of these mechanisms are inherently accounted for in a 3D numerical solution of the wave equations. The last mechanism, which is the purpose of this study, is through the anelastic effects accounted for through Q and caused by individual particle response at the atomic level, which can also constitute a good portion of the attenuated energy.

The quality factor Q is the measure of how close the rheology of a medium resembles that of an ideal elastic case. It is defined as

$Q = 2\pi E/\delta E$, where $\delta E/E$ is the fraction of energy lost per cycle [2]. The higher the value of Q (less energy lost) in a certain medium, the closer it would be to an ideal elastic rheology. As shown in several studies [15,18,25], the value of Q is generally constant over the typical seismic frequency range (5–40 Hz). As it is not possible to separate S- and P-waves at small scales, a single value of Q is used for both S- and P-waves in this study. The Q value is estimated by running the forward simulation for several predefined Q values, and then comparing the amplitude versus offset (AVO) curves with that of the actual field seismograms (see section of field data application for details).

2.2. Model updating

The steepest descent gradient method is used to minimize the misfit function and update material properties *Vs* and *Vp*. The misfit function $E(\boldsymbol{m})$ is defined as:

$$E(\boldsymbol{m}) = \frac{1}{2}\Delta\boldsymbol{u}^t\Delta\boldsymbol{u} \tag{3}$$

Where $\Delta\boldsymbol{u}$ denotes the wavefield displacement residuals between estimated data (solution of Eq. (1)) and field data for all the shots and receivers. The model $\boldsymbol{m}$ consists of *Vs* and *Vp* of all cells. *Vs* and *Vp* are wave velocities of viscoelastic medium (relaxed mechanism), which are smaller than those of elastic medium (unrelaxed mechanism). The phase velocities are related to the attenuative moduli as:

$$M = \lambda + 2\ \mu = \rho V_p^2, \quad \text{and} \quad \mu = \rho V_s^2 \tag{4}$$

As developed by Trinh et al. [28] and Yang et al. [33], the gradient of the misfit function for viscoelastic waves includes two terms (e.g. Eq. 20 from Ref. [28]). The first term related to strains is identical to that of elastic waves [4,22,27]. The second term related to memory variables is small compared to the first term, and can be neglected as noted by Trinh et al. [28]. By neglecting the term related to memory variables, the gradients of the misfit function with respect to attenuative Lame's parameters are calculated from the forward and backward wave-fields as:

$$\delta\lambda = -\sum_{i=1}^{NS}\int_0^T dt\left[\left(\frac{\partial u_x}{\partial x}+\frac{\partial u_y}{\partial y}\right)\left(\frac{\partial \psi_x}{\partial x}+\frac{\partial \psi_y}{\partial y}\right)+\left(\frac{\partial u_x}{\partial x}+\frac{\partial u_z}{\partial z}\right)\left(\frac{\partial \psi_x}{\partial x}+\frac{\partial \psi_z}{\partial z}\right)+\left(\frac{\partial u_y}{\partial y}+\frac{\partial u_z}{\partial z}\right)\left(\frac{\partial \psi_y}{\partial y}+\frac{\partial \psi_z}{\partial z}\right)\right] \tag{5}$$

$$\delta\mu = -\sum_{i=1}^{NS}\int_0^T dt\left[\begin{array}{l}\left(\frac{\partial u_x}{\partial y}+\frac{\partial u_y}{\partial x}\right)\left(\frac{\partial \psi_x}{\partial y}+\frac{\partial \psi_y}{\partial x}\right)+\left(\frac{\partial u_x}{\partial z}+\frac{\partial u_z}{\partial x}\right)\left(\frac{\partial \psi_x}{\partial z}+\frac{\partial \psi_z}{\partial x}\right)\\ \quad+\left(\frac{\partial u_y}{\partial z}+\frac{\partial u_z}{\partial y}\right)\left(\frac{\partial \psi_y}{\partial z}+\frac{\partial \psi_x}{\partial z}\right)\\ \quad\quad+2\left(\frac{\partial u_x}{\partial x}\frac{\partial \psi_x}{\partial x}+\frac{\partial u_y}{\partial y}\frac{\partial \psi_y}{\partial y}+\frac{\partial u_z}{\partial z}\frac{\partial \psi_z}{\partial z}\right)\end{array}\right]$$

Where *NS* is the number of shots, *T* is the total recording time, u_i and ψ_i $(i = x, y, z)$ are the forward and backward particle displacement for each cell in the *i*-direction, respectively. It is noted that the material anelasticity is inherently accounted in the gradients through the wavefield attenuation and propagation velocities (smaller than elastic velocities). Applying the chain rule to Eq. (4), the gradients in Eq. (5) are related to those of the velocities *Vs* and *Vp* as:

$$\delta V_P = 2\rho V_P\delta\lambda \tag{6}$$

$$\delta V_S = -4\rho V_S\delta\lambda + 2\rho V_S\delta\mu$$

Radial tapering at the source/receiver locations, linear tapering with depth, and Tikhonov regularization are then used for gradient precondition to reduce inversion artifacts and better resolve deeper structures. Finally, *Vs* and *Vp* of cells at iteration $n+1$ is updated from iteration n as:

$$V_P^{n+1} = V_P^n - \alpha_P\delta V_P$$

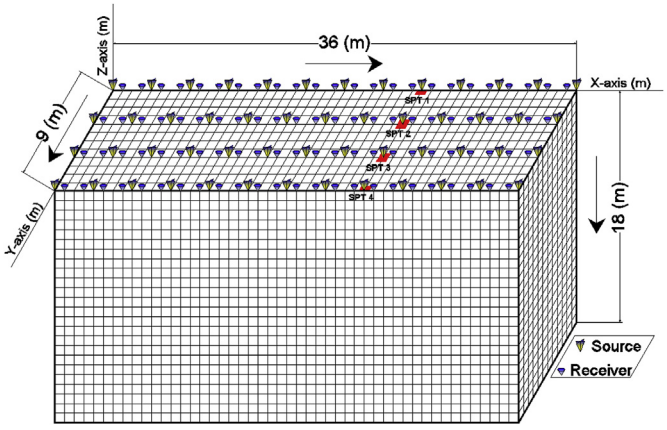

Fig. 1. True-scale meshing and test configuration used for both synthetic and field experiments. Four standard penetration tests (SPT, red rectangle) were conducted at x = 24 m on each of receiver lines for verification of seismic results. (For interpretation of the references to colour in this figure legend, the reader is referred to the Web version of this article.)

$$V_S^{n+1} = V_S^n - \alpha_S\delta V_S \tag{7}$$

Where α_P, α_S are optimal step lengths, which are determined by parabola fitting [20]. The gradient of *Vp* is scaled (e.g. max (δV_P)/max (V_P) = max (δV_S)/max (V_S)) to determine one optimal step length, which is then scaled accordingly for both α_P and α_S. The analysis stops when no optimal step length is found, or when the predefined maximum number of iterations is reached. More details on the gradient precondition can be found in Ref. [19].

3. Application on synthetic data

The 3D viscoelastic FWI algorithm was first tested on a synthetic dataset to assess its validity and capability. The synthetic dataset was created by the viscoelastic finite-difference forward solver SOFI3D, and then fed into the inversion algorithm as if they were field data. The viscoelastic forward simulation used in the creation of the synthetic dataset and in the inversion analysis uses the same quality factors ($Q_s = Q_P = 8$), and therefore no quality factor estimation (e.g. amplitude versus offset analysis) is required at this stage.

Shown in Fig. 1 is the true to scale discretization and acquisition geometry used in the finite-difference analysis of the forward simulation. A test configuration of 52 sources (shots) at a 3 × 3 m grid and 96 receivers at a 3 × 1.5 m grid was used on the surface. The model of 18 × 36 × 9 m (depth × length × width) was discretized into a grid of 0.75 m spacing for the entire medium. The synthetic model consisted of 3 layers with the *Vs* of 400, 200 and 600 m/s (Fig. 2a, left), and *Vp* was calculated from *Vs* with a constant Poisson's ratio of 1/3 (Fig. 2a, right). The Ricker wavelet source was applied in the vertical direction, and generated waveform data were recorded for a total time of 0.9 s.

A 1D *Vs* profile linearly increased with depth from 400 m/s at the surface to 600 m/s at the bottom (18 m-depth) was used as the initial model for the inversion analysis. The initial *Vp* was twice of that of the initial *Vs* (Fig. 2b). Such an initial model could be established via a spectral analysis of measured data as detailed later in the field data application. The entire inversion process was carried out in two stages. The first inversion stage began with the initial model on waveform data of 5–20 Hz with the center frequency of 12 Hz. The second inversion stage was on waveform data of 5–30 Hz with the center frequency of 20 Hz, using the result of the first stage as the initial model. *Vs* and *Vp* were updated simultaneously during inversion analysis, while the mass density of 1800 kg/m^3 was kept constant. Both inversion stages stopped at 20 iterations (the predefined max number of iterations). The complete analysis took about 18 h on a workstation computer with 8 cores

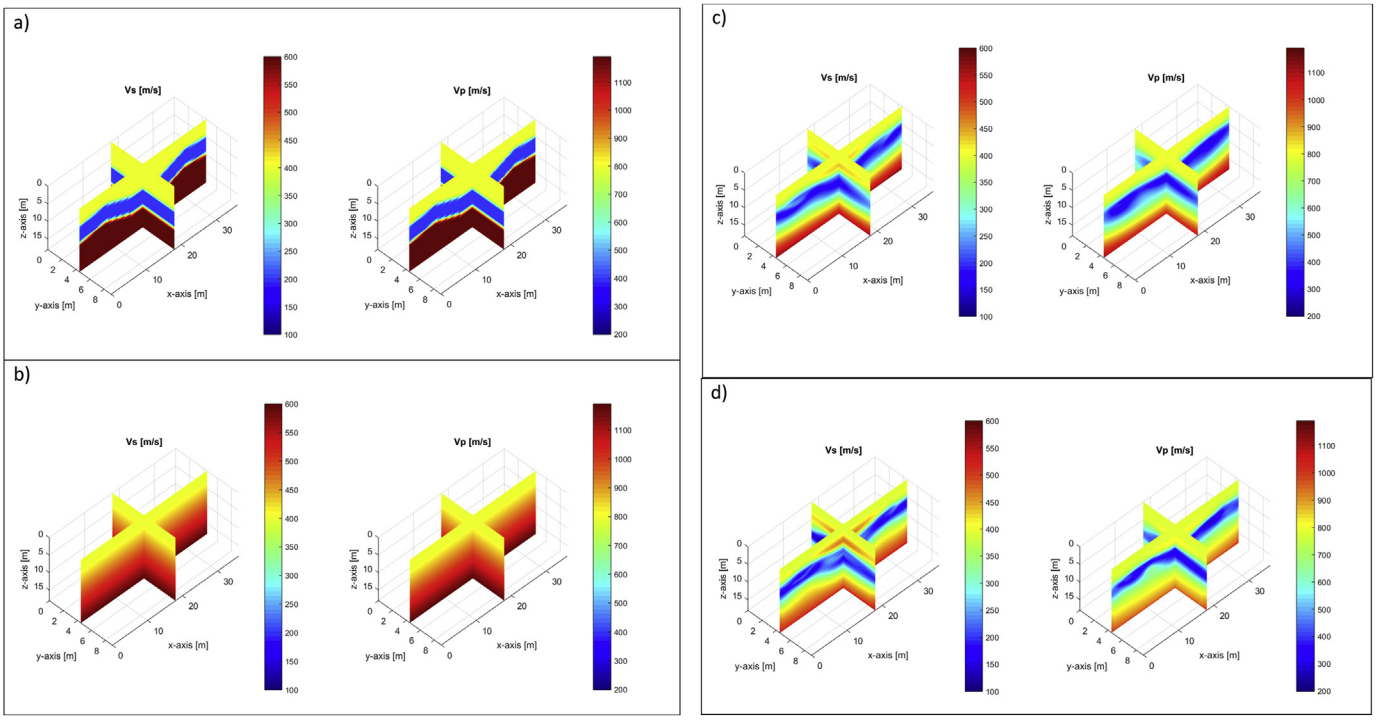

Fig. 2. Synthetic model: distribution of *Vs* and *Vp*: a) true model used to generate synthetic data for inversion analysis; b) initial model used at the beginning of inversion; and c) and d) inverted models with data at 5–20 Hz and 5–30 Hz, respectively.

running at 3.8 GHZ each, 64 GB of RAM and 1 TB of hard drive storage.

Fig. 3 shows the normalized error for the two inversion stages versus iterations. The overall error has consistently decreased during each stage to a final value of less than 0.01 at the end of the second stage. Shown in Fig. 4 is the waveform comparison for a sample shot between the observed data and the estimated data associated with the initial (Fig. 4a) and the final inverted results (Fig. 4b and c) at the end of each inversion stage. Apparently, the waveform match improved significantly during the first inversion stage. The observed data and estimated data at the end of each inversion stage are most identical. No cycle skipping (matching of wrong peaks) is observed, showing that the selected 1D initial model is sufficient.

The inverted result for the first stage at 5–20 Hz is shown in Fig. 2c. Comparing to the true model (Fig. 2a), the three layers are clearly recovered and defined with separate distinguishable boundaries. Particularly, the low-velocity second layer is clearly imaged without any prior information required in the initial model. The inverted result for the second stage at 5–30 Hz is shown in Fig. 2d. Adding higher frequency data helped improving the layer boundaries; however, no other discernible improvement is observed.

4. Application on field data

After obtaining the encouraging result on synthetic data, the 3D viscoelastic FWI algorithm was applied on a field dataset collected from a dry retention pond in Gainesville, Florida, USA (Fig. 5a). Similar to the synthetic analysis, a test configuration of 52 shots and 96 receivers (Fig. 1) was used for the field experiment. A propelled energy generator (Fig. 5b) is used to generate seismic wave-fields. The field experiment was carried out in two stages. In the first stage, 48 4.5-Hz vertical

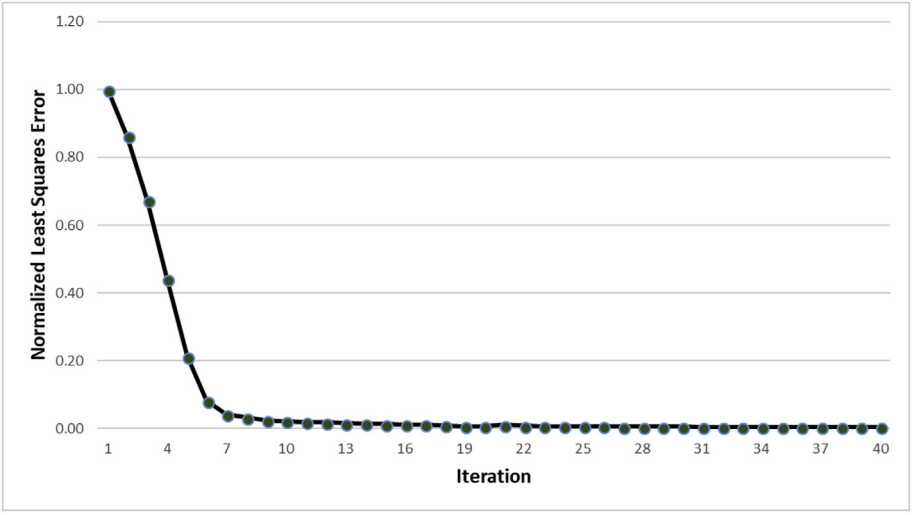

Fig. 3. Normalized least squares error versus iterations for both inversion stages at 5–20 Hz and 5–30 Hz.

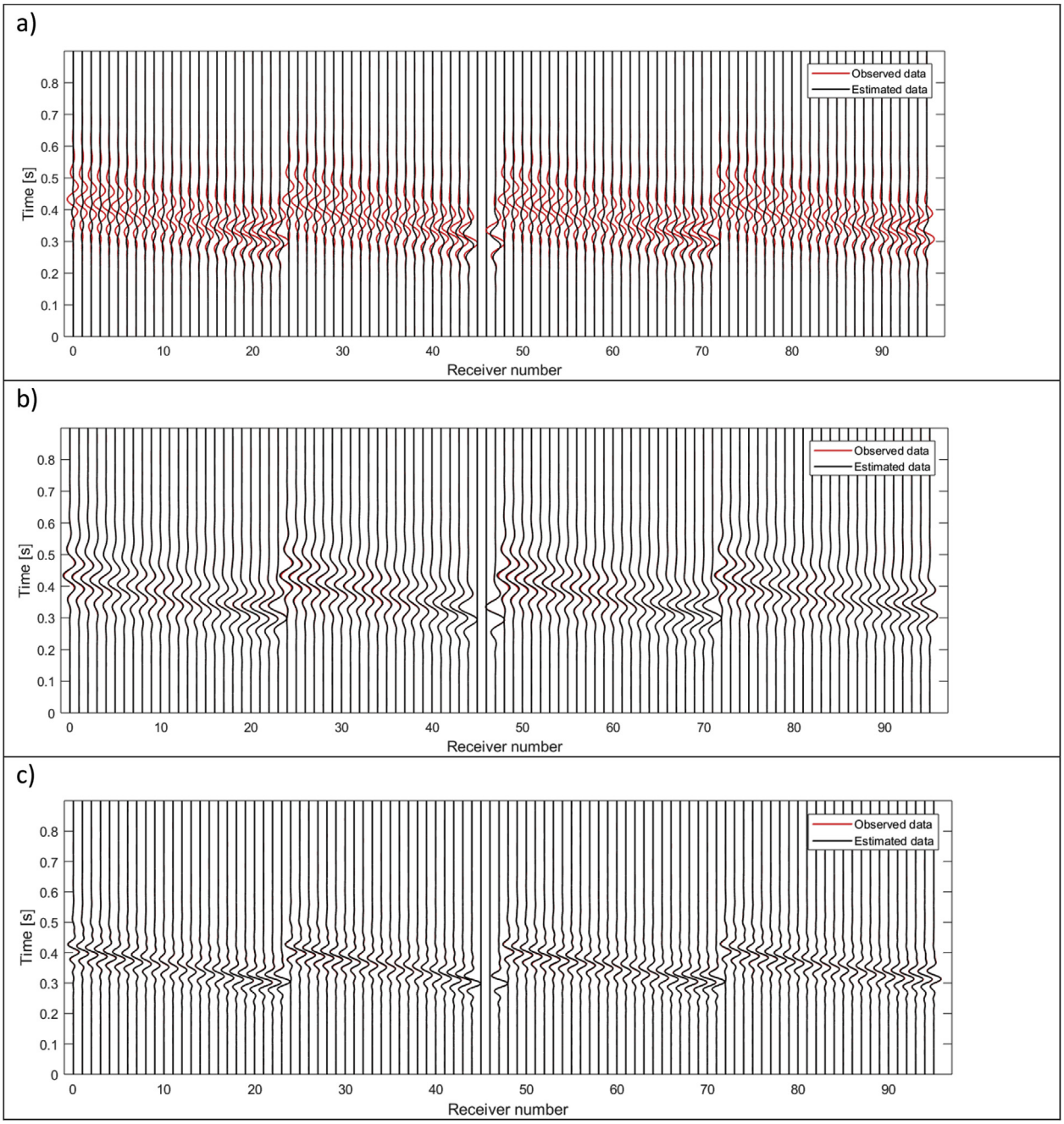

Fig. 4. Synthetic model: waveform comparison between the observed data and estimated data associated with the initial model (a), final inverted model at the 5–20 Hz analysis (b), and final inverted model at the 5–30 Hz analysis (c).

geophones were placed on a half of the receiver grid, and 52 shots were applied for the entire source grid. In the second stage, the 48 receivers were moved to the other half and the process was repeated. Given the uniformity of the generated source signatures (same dropped weight and height), the collected wave-fields from the two stages were simply combined to form 96-channel shot gathers. Four standard penetration tests (SPT) were also conducted at distance x = 24 m on each of geophone lines for verification of seismic results. This same dataset had been analyzed by a 3D elastic FWI algorithm [19], and the results are also included in this paper for comparison.

As presented by Nguyen and Tran [19], a 1D initial model was developed via spectral analysis of the measured data for a sample shot and one line of 24 geophones (Fig. 6). Rayleigh wave velocities (*Vr*) were determined from 250 to 400 m/s at the frequency range of 12–50 Hz. As *Vs* is similar to *Vr*, the *Vs* near the ground surface associated with high frequency data was known to be approximately 250 m/s. Consequently, the half space with *Vs* of 400 m/s was assumed at the start at a half of maximum wavelength associated with data at 12 Hz or a depth of 16.7 m (velocity/frequency/2 = 400/12/2 = 16.7 m). Similar to the case of synthetic model, the initial model (Fig. 7a) was established having *Vs* increasing with depth from 250 m/s at the surface to 400 m/s (*Vs* of the half space) at the bottom of the model. The depth of model was taken as a half of the longer dimension of test area (or 18 m) to maintain good signal coverage in the analyzed domain. The *Vp* was estimated from *Vs* and a constant Poisson's ratio of 1/3 for the entire medium, which was taken as the characteristic value of the range from ¼ to ½ for general soils.

Before running the actual inversion on the field data, an amplitude

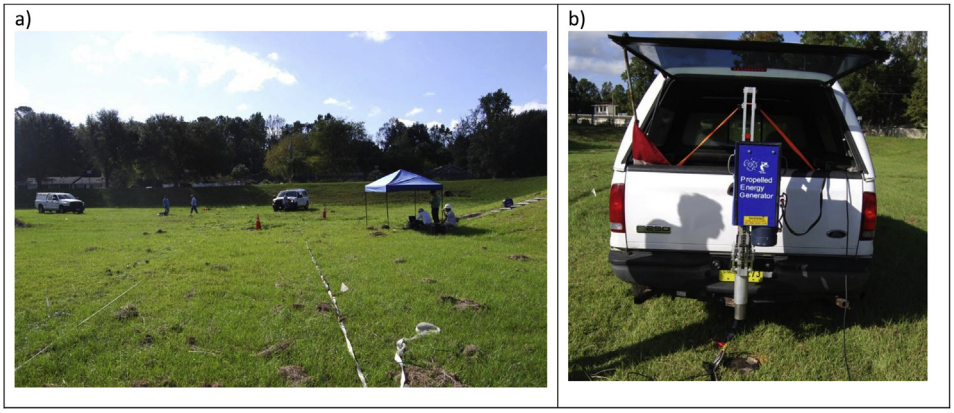

Fig. 5. Field experiment: a) test site and b) propelled energy generator.

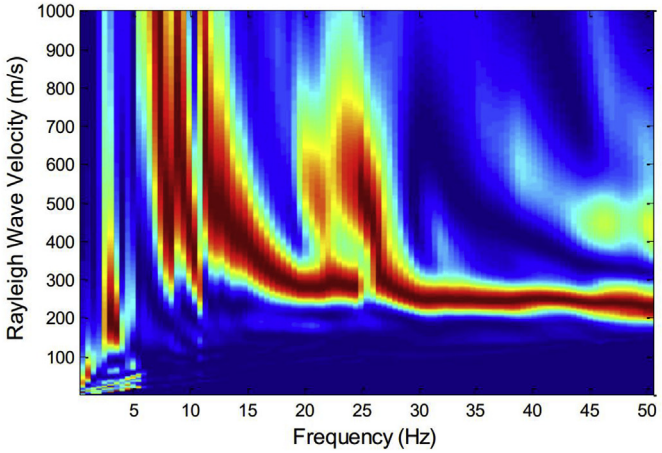

Fig. 6. Field experiment: spectral analysis of measured data for one sample shot and one line of 24 geophones.

versus offset (AVO) analysis was carried out to determine the quality factor (Q). Eight different Q values from 0.5 to 15 (as shown in Fig. 8) were assumed. Each value was used in the viscoelastic forward simulation on the initial model (Fig. 7a) to generate synthetic wave-field for one shot at the beginning (x = 0) of each receiver lines. The generated wave-fields were recorded along the 4 receiver lines, and the maximum absolute amplitudes were determined. To eliminate the near-field effects, the first 5 receivers from the source were omitted from the AVO analysis, and the results are normalized with the maximum amplitude of the remaining 19 receivers for each line. The normalized AVO results of the forward simulation from all 4 receiver lines were then averaged, and plotted in Fig. 8 along with the AVO curve of the field data. The field data AVO almost lies between those of synthetic data associated with Q = 5 and 10, suggesting the Q value is from 5 to 10.

To double check the Q value, the least squares error between the amplitudes of the simulated and field data was then calculated for each quality factor as shown in Fig. 9. The value of Q = 8 provided the best depiction of the actual field anelasticity with the minimum error, and thus was selected as the quality factor and fixed during inversion analysis. As noted by Meier et al. [16], Q values lower than 10 not only have an influence on the amplitude, but also significantly change the dispersion behavior of the Rayleigh waves. Therefore, only adjusting the amplitude of waveform data to account for anelastic effects, e.g. multiplying it with a correction factor [19], may not be sufficient. In this case, the viscoelastic wave simulation is required to accurately account for the influences on the amplitude and dispersion (phase change and wave mode conversions). The viscoelastic simulation allows the inversion algorithm to account for the intrinsic attenuation of the entire medium in the gradient vectors (Eq. (5)) through the forward and backward wave propagation rather than only waveform residuals. This potentially leads to better characterizing of subsurface features.

Similar to the synthetic case, the inversion analysis was carried out in two stages. The first stage was at 5–20 Hz on the initial model (Fig. 7a), and the second stage was at 5–30 Hz using the inverted result from the first stage as the initial velocity input. For the forward simulation, source signatures for each shot location were estimated by deconvolution of the measured data with the Green's function, which was explicitly calculated using the forward simulation with an assumed Ricker wavelet source [29]. The source signatures were updated at the beginning of each iteration to account for the change of the Green's function during inversion due to updated model parameters.

The entire medium of 18 × 36 × 9 m (depth × length × width) was discretized into 13,824 cells of 0.75 m (Fig. 1). *Vs* and *Vp* of cells were updated simultaneously during inversion. The mass density of 1800 kg/m^3 was selected as a typical value for general soils, and fixed during inversion. The termination criterion was set at the point where the predefined maximum number of iterations was reached or no optimal step length was found. Both inversion runs stopped at the predefined number of iterations (20 iterations). The entire analysis time for the two stages was about 19 h on the same computer that was used in synthetic wave-field inversion analysis.

Fig. 10 shows the normalized least squares error for both inversion stages. The error has consistently decreased throughout the first 20 iterations (5–20 Hz), increased at the beginning of the second stage (5–30 Hz), and then decreased to 0.78 at the end of the second stage. The jump in the normalized error at the beginning of the second stage is due to the sudden increase in the information content of the higher frequency bandwidth while the model is not yet ready to fit the higher frequency data.

Shown in Fig. 11 is the waveform comparison between the observed data and estimated data associated with the initial model and final inverted models at the two inversion stages. Unlike the synthetic case, the observed and initial estimated data at 5–20 Hz (Fig. 11a) agree well, suggesting the initial model well represents the true soil profile. Thus it is more difficult to improve the waveform match, and the error only decreased 22% from 1.0 to 0.78 for the entire inversion. Nevertheless, the overall waveform match did improve for most of channels as shown in Fig. 11b. The observed data and the estimated data associated with the final inverted result at 5–30 Hz is shown in (Fig. 11c), where the good agreement is also observed.

The final inverted results at the end of each frequency stage are shown in Fig. 7 b and 7c. The *Vs* profile (Fig. 7c, left) consists of softer layers (*Vs* ~ 150–300 m/s) with a buried low-velocity zone at about 5-m depth, underlain by a stiffer layer (*Vs* ~ 400 m/s). The *Vp* profile (Fig. 7c, right) is consistent with the *Vs* profile. Increasing the frequency content has revealed a low velocity zone to the left side of the medium

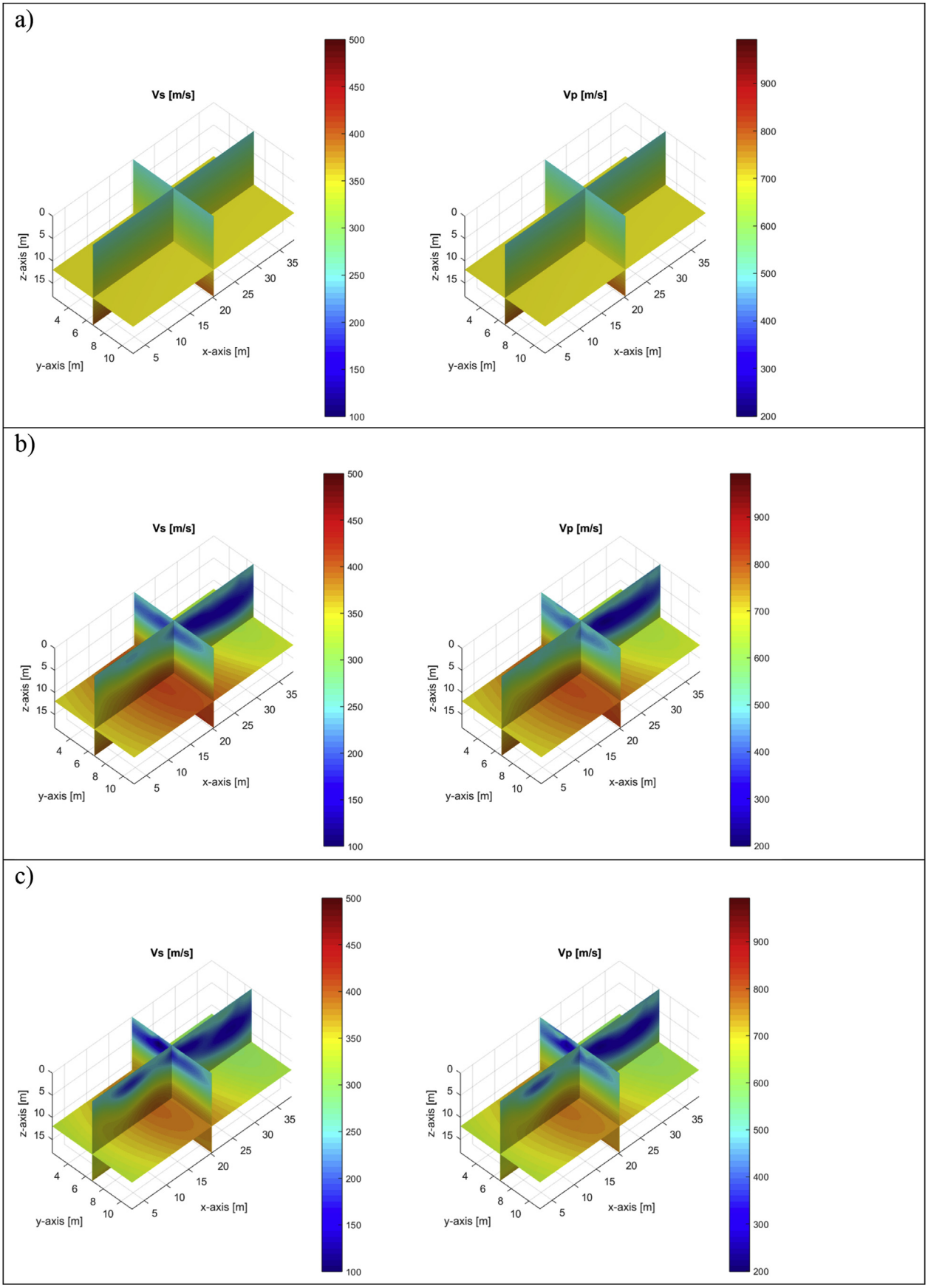

Fig. 7. Field experiment: distribution of *Vs* and *Vp*: a) initial model used at the beginning of inversion; and b) and c) inverted models with data at 5–20 Hz and 5–30 Hz, respectively.

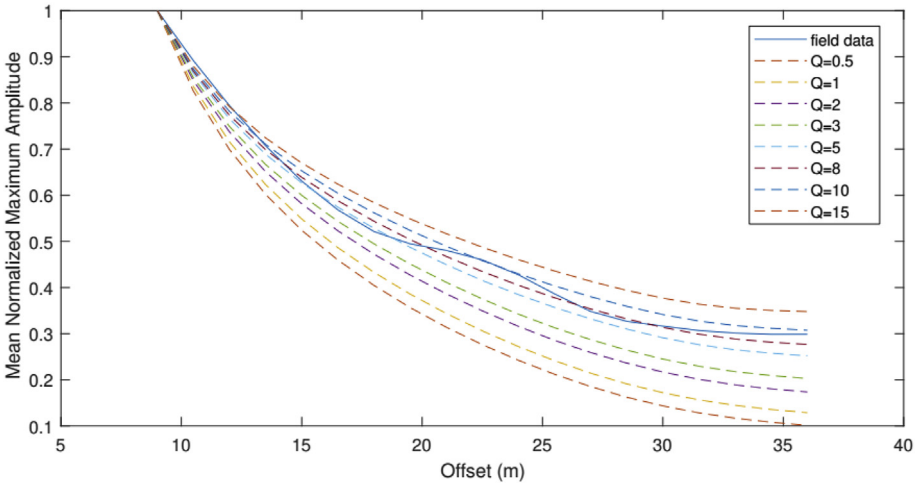

Fig. 8. Field experiment: mean normalized maximum waveform amplitude versus source-receiver offset (AVO).

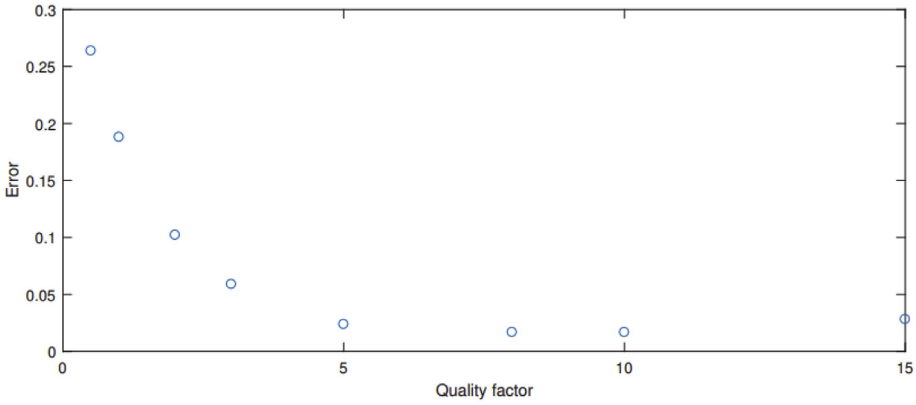

Fig. 9. Field experiment: error versus quality factor. The error measures the difference between the mean normalized maximum amplitudes of the simulated and field data for each quality factor.

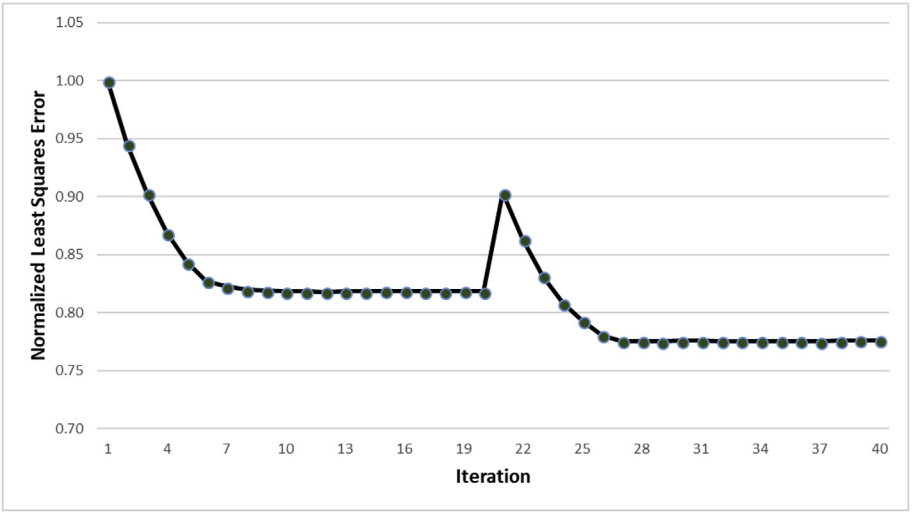

Fig. 10. Field experiment: normalized least squares error for the first inversion stage at 5–20 Hz (iterations 1 to 20) and the second inversion stage at 5–30 Hz (iterations 21 to 40). The error increases at higher frequencies because the model is not yet appropriate to produce the recorded wave propagation of shorter wavelengths.

(Fig. 7 c), which had not been identifiable from the first stage of the inversion analysis at 5–20 Hz (Fig. 7 b). This is due to the smaller wavelengths at higher frequencies that reveals finer structures in the gradient. Comparing the initial velocity profile (Fig. 7a) with the final inverted result (Fig. 7c), the *Vs* and *Vp* profiles changed significantly during inversion even with only 22% of the error decrease. For better viewing of lateral variation, Fig. 12 shows vertical slices of *Vs* along 4 receiver lines at y = 0, 3, 6, and 9 m, together with the 4 SPT locations at x = 24 m. Consistent variation of the *Vs* profile is observed along y direction.

For verification, the initial *Vs* values, the final inverted *Vs* values at 5–30 Hz, and SPT N-values at 4 locations are shown together in Fig. 13. The depths of four SPTs are about 21-m depth. Again, the *Vs* profile changed significantly during inversion analysis, particularly at depths

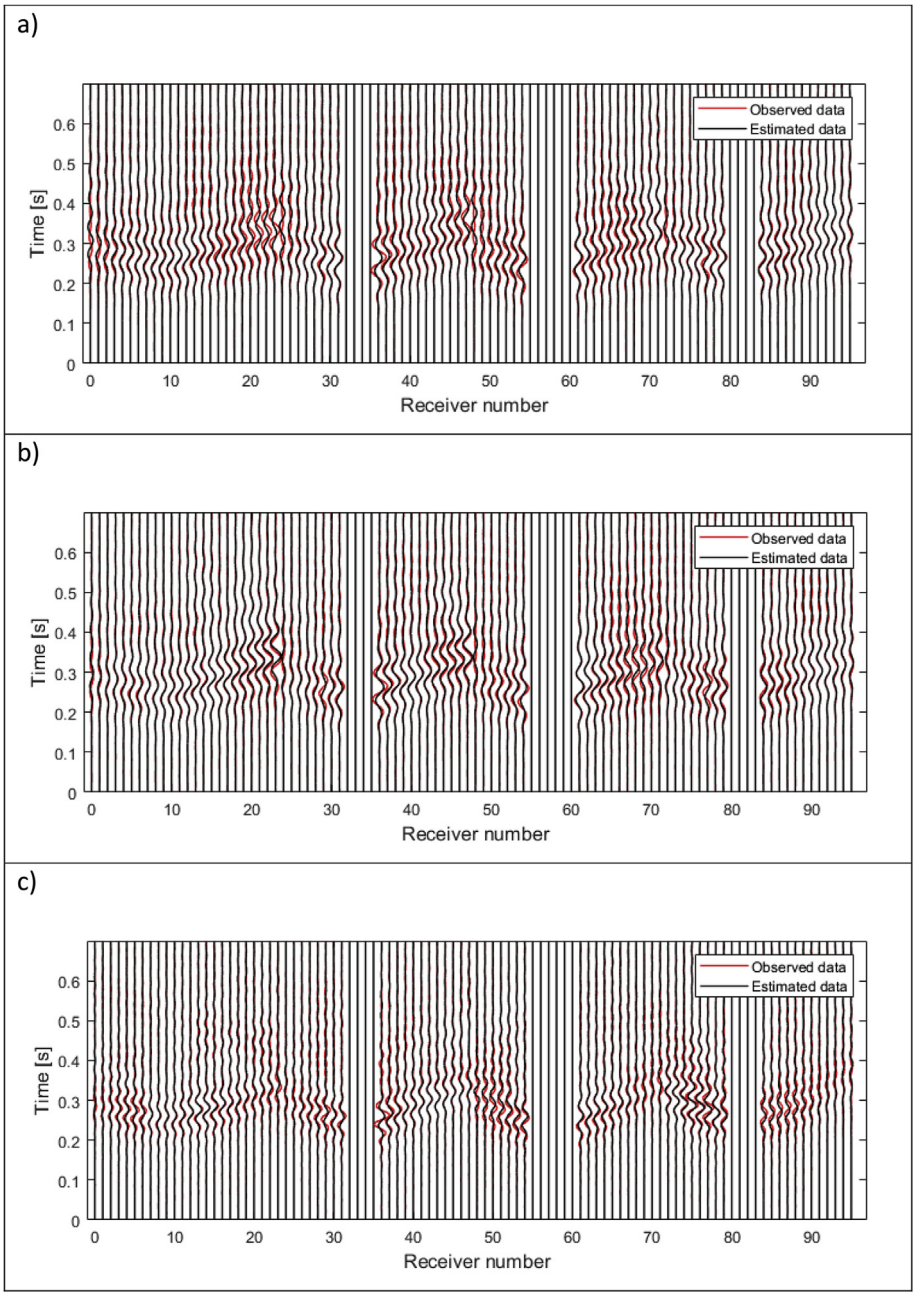

Fig. 11. Field experiment: waveform comparison between the observed data and estimated data associated with the initial model (a), final inverted model at the 5–20 Hz analysis (b), and final inverted model at the 5–30 Hz analysis (c).

less than 10 m. The final inverted *Vs* and SPT results agree at all four locations. Both show soft materials from 0 to 5-m depth, linearly increasing stiffness with depth from 5 to 10-m depth, and stiffer materials below 10-m depth. The low-velocity zone at about 5-m depth identified by the waveform analysis is confirmed by the SPT results, particularly at the SPT-3 and SPT-4 locations. There is discrepancy between the *Vs* (higher values) and SPT N-values at depths less than 2 m of SPT-1 and SPT-2. The discrepancy could be due to local compactions of soil during seismic testing by the truck carrying the seismic source, or more likely due to inversion artifacts near source locations. Also, the SPT N-values appear more erratic than *Vs* values, because N-values represent more local properties (over 0.3 m vertical distance of SPT tube) than do *Vs* values. The *Vs* values are average within cell volumes ($0.75 \times 0.75 \times 0.75$ m each) and partially constrained by those of adjacent cells due to Tikhonov regularization that produces smooth inversion results.

Results from this seismic dataset analyzed by a 3D elastic FWI had been reported in details by Nguyen and Tran [19], in which the same initial model and frequency content were used. The inverted *Vs* from the elastic inversion at the 4 SPT locations are also included in Fig. 13 for comparison. Apparently, both viscoelastic and elastic methods produce good results for this dataset. However, the inverted *Vs* from viscoelastic method are more consistent with the SPT N-values in both trend and magnitudes at all the 4 SPT locations. The 3D elastic FWI tends to overshoot the low-velocity zones, particularly at SPT-1 and SPT-4. The superiority of the viscoelastic approach is mostly attributed to the accurate simulation of the intrinsic attenuation of the entire medium, which is incorporated in the gradient vectors (Eq. (3)) through the forward and backward wave propagation rather than only waveform residuals.

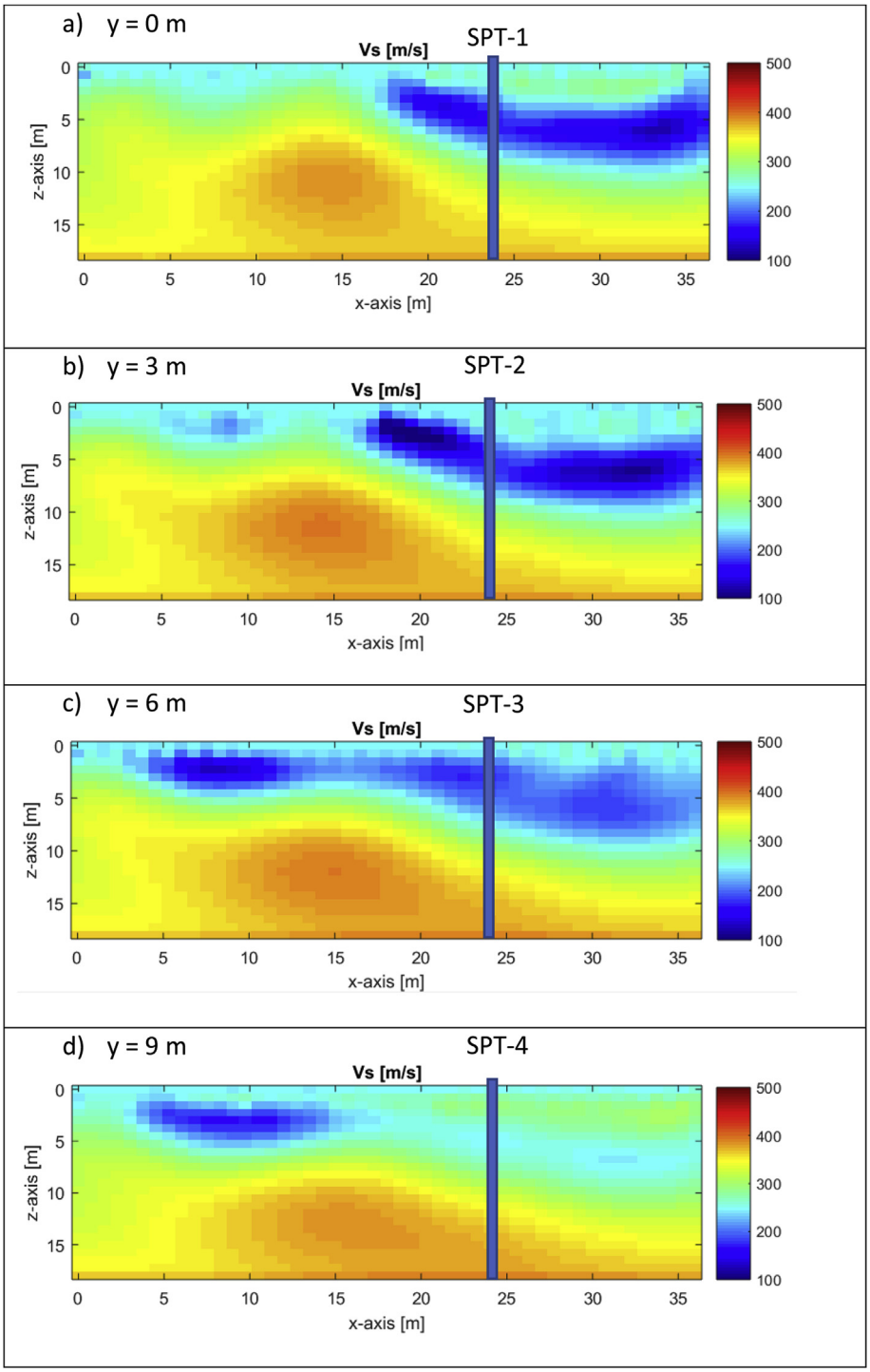

Fig. 12. Field experiment: inverted *Vs* and SPT locations along four receiver lines at y = 0, 3, 6, and 9 m

5. Conclusion

A 3D viscoelastic FWI method is presented for the geotechnical site characterization. It is based on a solution of 3D viscoelastic wave equations and the adjoint-state inversion approach. The capability of the method was tested on both synthetic and field datasets. The results from synthetic dataset suggest that the presented waveform inversion can accurately characterize variable high- and low-velocity subsurface layers. For the field data, it is shown that a basic amplitude versus offset (AVO) analysis can provide a good estimation of the anelastic parameter Q required for viscoelastic wave simulation. The viscoelastic simulation eliminates the need for adjusting simulated waveform data to account for anelasticity effects, and therefore provides a more straightforward and realistic scenario for the application of the inversion algorithm to the field data. Both *Vs* and *Vp* of variable soil layers are characterized to 18-m depth with only surface-based seismic data. There is good agreement between the *Vs* and SPT N-values, including the identification of a buried low-velocity zone at 5-m depth. Results from the viscoelastic inversion are more consistent to the SPT N-values than those from the elastic inversion.

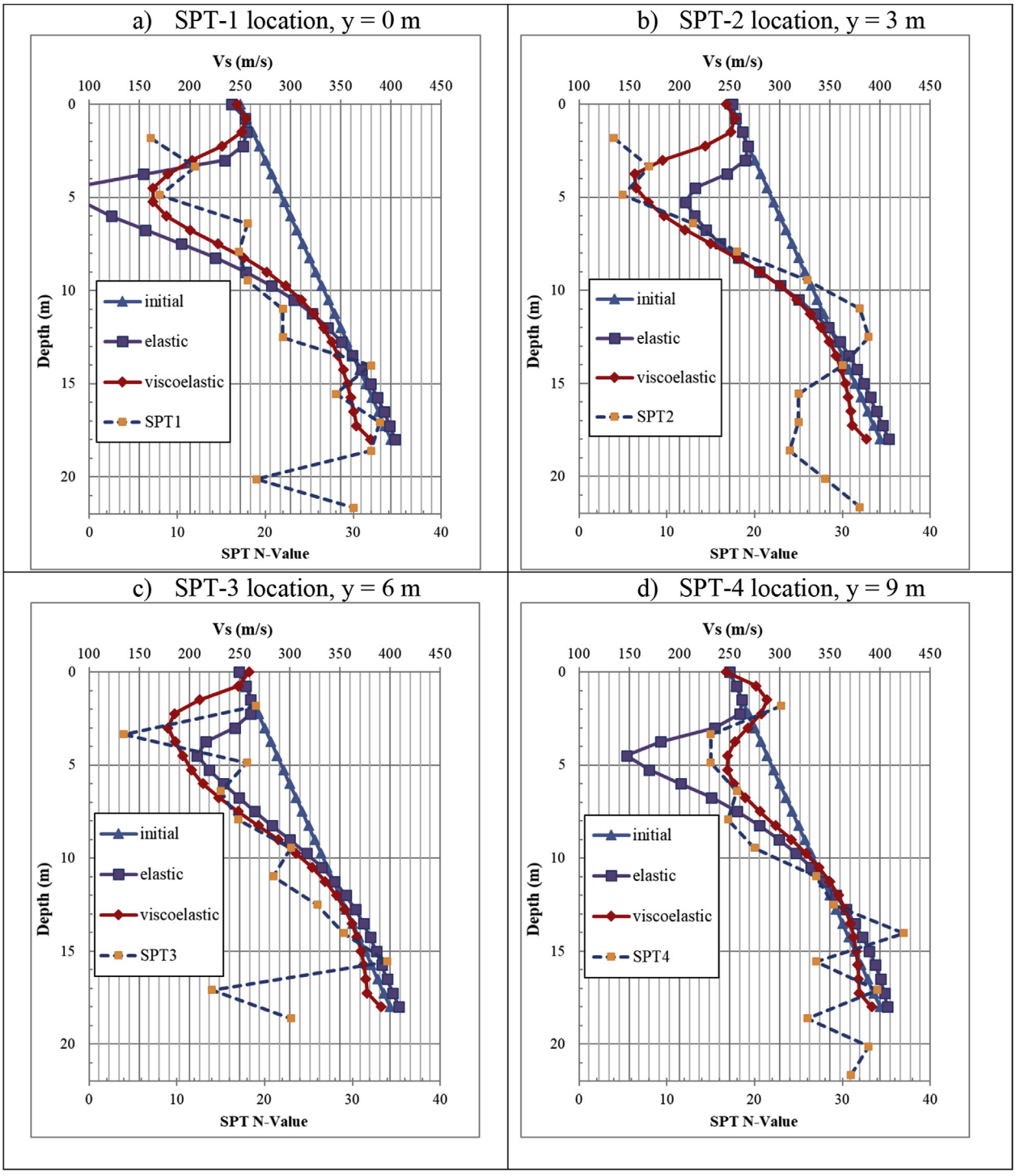

Fig. 13. Comparison between *Vs* and SPT N-values at the 4 invasive test locations.

Acknowledgments

This study was financially supported by the National Science Foundation: grant CMMI-1637557. The support is greatly acknowledged. The authors would like to thank the FDOT State Materials Office in Gainesville, FL for providing access to the test site and conducting the SPT data.

Appendix A. Supplementary data

Supplementary data to this article can be found online at https://doi.org/10.1016/j.soildyn.2019.04.005.

References

[1] Ben-Hadj-Ali H, Operto S, Virieux J. Velocity model building by 3D frequency-domain, full-waveform inversion of wide-aperture seismic data3D full-waveform tomography. Geophysics 2008;73:VE101–17.
[2] Blanch JO, Robertsson JO, Symes WW. Modeling of a constant Q: methodology and algorithm for an efficient and optimally inexpensive viscoelastic technique. Geophysics 1995;60:176–84.
[3] Bohlen T. Parallel 3-D viscoelastic finite difference seismic modelling. Comput Geosci 2002;28:887–99.
[4] Butzer S, Kurzmann A, Bohlen T. 3D elastic full-waveform inversion of small-scale

heterogeneities in transmission geometry. Geophys Prospect 2013;61:1238–51.
[5] Carcione JM, Kosloff D, Kosloff R. Wave propagation simulation in a linear viscoelastic medium. Geophys J Int 1988;95:597–611.
[6] Dokter E, Köhn D, Wilken D, De Nil D, Rabbel W. Full-waveform inversion of SH- and Love-wave data in near-surface prospecting. Geophys Prospect 2017;65:216–36.
[7] Epanomeritakis I, Akçelik V, Ghattas O, Bielak J. A Newton-CG method for large-scale three-dimensional elastic full-waveform seismic inversion. Inverse Probl 2008;24:034015.
[8] Fabien-Ouellet G, Gloaguen E, Giroux B. Time domain viscoelastic full waveform inversion. Geophys J Int 2017;209:1718–34.
[9] Fathi A, Kallivokas LF, Poursartip B. Full-waveform inversion in three-dimensional PML-truncated elastic media. Comput Methods Appl Mech Eng 2015;296:39–72.
[10] Fathi A, Poursartip B, Stokoe Ii KH, Kallivokas LF. Three-dimensional P-and S-wave velocity profiling of geotechnical sites using full-waveform inversion driven by field data. Soil Dynam Earthq Eng 2016;87:63–81.
[11] Fichtner A, Kennett BL, Igel H, Bunge H-P. Full seismic waveform tomography for upper-mantle structure in the Australasian region using adjoint methods. Geophys J Int 2009;179:1703–25.
[12] Goutbeek F, Dost B, Van Eck T. Intrinsic absorption and scattering attenuation in the southern part of The Netherlands. J Seismol 2004;8:11–23.
[13] Groos L, Schäfer M, Forbriger T, Bohlen T. Application of a complete workflow for 2D elastic full-waveform inversion to recorded shallow-seismic Rayleigh waves. Geophysics 2017;82:R109–17.
[14] Ha W, Kang S-G, Shin C. 3D Laplace-domain waveform inversion using a low-frequency time-domain modeling algorithm. Geophysics 2015;80:R1–13.
[15] Mcdonal F, Angona F, Mills R, Sengbush R, Van Nostrand R, White J. Attenuation of shear and compressional waves in Pierre shale. Geophysics 1958;23:421–39.
[16] Meier T, et al. Investigating surficial alterations of natural stone by ultrasonic surface measurements. Masini N, Soldovieri F, editors. Sensing the past. Geotechnologies and the Environment, vol. 16. Cham: Springer; 2017.
[17] Métivier L, Brossier R, Mérigot Q, Oudet E, Virieux J. An optimal transport approach for seismic tomography: application to 3D full waveform inversion. Inverse Probl 2016;32:115008.
[18] Murphy Iii WF. Effects of partial water saturation on attenuation in Massilon sandstone and Vycor porous glass. J Acoust Soc Am 1982;71:1458–68.
[19] Nguyen TD, Tran KT. Site characterization with 3D elastic full-waveform tomography. Geophysics 2018;83:R389–400.
[20] Nocedal J, Wright S. Least-squares problems. Numerical optimization 2006:245–69.
[21] Plessix RE. Three-dimensional frequency-domain full-waveform inversion with an iterative solver. Geophysics 2009;74:WCC149–57.
[22] Plessix RE. A review of the adjoint-state method for computing the gradient of a functional with geophysical applications. Geophys J Int 2006;167:495–503.
[23] Robertsson JO, Blanch JO, Symes WW. Viscoelastic finite-difference modeling. Geophysics 1994;59:1444–56.
[24] Sirgue L, Barkved O, Dellinger J, Etgen J, Albertin U, Kommedal J. Thematic set: full waveform inversion: the next leap forward in imaging at Valhall. First Break 2010;28:65–70.
[25] Spencer JW. Stress relaxations at low frequencies in fluid-saturated rocks: attenuation and modulus dispersion. J Geophys Res: Solid Earth 1981;86:1803–12.
[26] Tape C, Liu Q, Maggi A, Tromp J. Seismic tomography of the southern California crust based on spectral-element and adjoint methods. Geophys J Int 2010;180:433–62.
[27] Tromp J, Tape C, Liu Q. Seismic tomography, adjoint methods, time reversal and banana-doughnut kernels. Geophys J Int 2005;160:195–216.
[28] Trinh PT, Brossier R, Métivier L, Tavard L, Virieux J. Efficient time-domain 3D elastic and viscoelastic full-waveform inversion using a spectral-element method on flexible Cartesian-based mesh. Geophysics 2018;84(1):R75–97.
[29] Tran KT, Luke B. Full waveform tomography to resolve desert alluvium. Soil Dynam Earthq Eng 2017;99:1–8.
[30] Vigh D, Kapoor J, Moldoveanu N, Li H. Breakthrough acquisition and technologies for subsalt imaging. Geophysics 2011;76:WB41–51.
[31] Virieux J, Operto S. An overview of full-waveform inversion in exploration geophysics. Geophysics 2009;74:WCC1–26.
[32] Warner M, Ratcliffe A, Nangoo T, Morgan J, Umpleby A, Shah N. Anisotropic 3D full-waveform inversion. Geophysics 2013;78(2):R59–80.
[33] Yang P, Brossier R, Métivier L, Virieux J. A review on the systematic formulation of 3D multiparameter full waveform inversion in viscoelastic medium. Geophys J Int 2016;207:129–49.